water

MDPI

Article

Synthesis of Ag-OMS Catalyst for Sunlight-Assisted Photodegradation of Crystal Violet Dye

Muhammad Saeed [1,*], Renzon Daniel Cosme Pecho [2], Sandeep Panchal [3], Sadeq K. Alhag [4], Laila A. Al-Shuraym [5], Khalid M. Al Syaad [6] and Usman Hanif Bhutta [1]

1 Department of Chemistry, Government College University Faisalabad, Faisalabad 38000, Pakistan
2 Department of Biochemistry, Universidad San Ignacio de Loyola (USIL), Lima 15024, Peru
3 Department of Civil Engineering, Government Polytechnic Mankeda, Agra 283102, Uttar Pradesh, India
4 Biology Department, College of Science and Arts, King Khalid University, Abha 63763, Saudi Arabia
5 Biology Department, Faculty of Science, Princess Nourah Bint Abdulrahman University, Riyadh 11564, Saudi Arabia
6 Biology Department, College of Science, King Khalid University, Abha 61413, Saudi Arabia
* Correspondence: msaeed@gcuf.edu.pk; Tel.: +92-346-9010903

Abstract: The contamination of water with organic pollutants, such as dyes, has become a serious threat to the environment. Therefore, the development of a cost-effective, eco-friendly, proficient, and visible-light-driven catalyst for the treatment of organic dye-contaminated wastewater has been a burning issue recently. Photocatalysis is suggested as a potential treatment technique for the eradication of organic pollutants. The 1D tunnel-structured manganese oxide octahedral molecular sieve (OMS) is a suitable substance to be tested as a visible-light-driven photocatalyst for the degradation of organic contaminants. However, the fast recombination of photoinduced charges (h^+/e^-) limits its photocatalytic application. The development of heterojunctions between OMS and other metals, such as Ag, is a suitable technique for improving the photocatalytic performance of OMS. In this study, Ag-OMS with plasmon-enhanced photocatalytic activity is reported for the photodegradation of crystal violet dye. Manganese oxide OMS was prepared by an acidic precipitation method using potassium permanganate, manganese acetate, and nitric acid as precursor materials. Ag nanoparticles were deposited on OMS using leaf extracts of *Calotropis gigantea*. The deposition of Ag enhanced the photocatalytic performance of OMS from 68 to 95%. The effects of Ag contents, catalyst dosage, and concentration of crystal violet dye on catalytic performance were explored as well. Approximately 100, 95, and 75% photodegradation of 50, 100, and 150 mg/L crystal violet dye was observed in 90, 120, and 120 min in the presence of 10% Ag-OMS, respectively. Excellent photocatalytic performance, low dose utilization, and reusability proved that Ag-OMS might have practical environmental applications.

Keywords: octahedral molecular sieves (OMS); photodegradation; crystal violet dye; heterojunction; reaction kinetics; wastewater treatment

check for updates

Citation: Saeed, M.; Pecho, R.D.C.; Panchal, S.; Alhag, S.K.; Al-Shuraym, L.A.; Al Syaad, K.M.; Bhutta, U.H. Synthesis of Ag-OMS Catalyst for Sunlight-Assisted Photodegradation of Crystal Violet Dye. *Water* **2023**, *15*, 2480. https://doi.org/10.3390/w15132480

Academic Editor: Urooj Kamran

Received: 10 June 2023
Revised: 28 June 2023
Accepted: 30 June 2023
Published: 6 July 2023

1. Introduction

Water is an obligatory part of everyday life and is used broadly for agriculture, energy, public hygiene, industrial purposes, and drinking. The rapid industrial development and increase in population caused a brutal escalation in environmental pollution by generating industrial effluents and waste materials [1–9]. The discharge of effluents from industries, such as textile, leather, paint, pulp, pharmaceuticals, food, cosmetics, etc. releases organic dyes and other pollutants into the environment, which causes a significant increase in the rate of contamination [10–12]. These orgasmic dyes badly affect living organisms due to their carcinogenic and chemically resistant nature. Therefore, it is crucial to develop methods and techniques for the elimination of these dyes from the environment [13–18]. Previously, the removal of these dyes was accomplished by various conventional methods.

These conventional methods include reverse osmosis, coagulation, flocculation, and the most commonly used adsorption method. Although these conventional methods were effective for the separation of pollutants from water, they were expensive and tedious. Furthermore, these methods were ineffective in completing the mineralization of the pollutants [19–21]. These important issues were overcome by the application of photocatalysis. Photocatalysis using transition metal oxides as catalysts is a facile and green technique for the treatment of dye-contaminated wastewater [22–24]. Photocatalysis emerged as a popular research area due to its effectiveness, low cost, and eco-friendly nature. Furthermore, this method removes organic pollutants by reducing toxic molecules to simple and harmless components [25–30]. Recently, manganese oxides and their composites have been extensively used as catalysts and adsorbents for the removal of organic pollutants from the aqueous system [31–37]. Manganese oxides exist in various crystal forms. The crystalline forms of manganese oxides have been classified into 1D tunnel structures, 2D layered structures, and 3D spinel structures. The crystalline phase of manganese oxides in all three structures consists of [MnO_6] octahedral units. The 1D tunnel structure of manganese oxide, called manganese oxide octahedral molecular sieve, has received extensive attention due to its superior catalytic performance [38–41]. There are three tunnel structures of manganese oxides called todorokite, cryptomelane, and pyrolusite (Figure 1). These structures are denoted as MnO (3 × 3), MnO (2 × 2), and MnO (1 × 1), respectively.

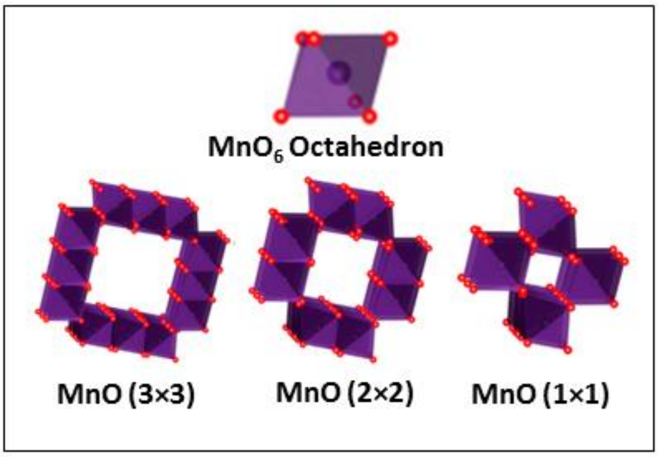

Figure 1. Tunnel structures of manganese oxides.

The [MnO_6] octahedron forms single, double, or triple chains through edge and/or angle sharing, and then the chains form a square hollow tunnel in an approximately orthogonal manner [42–44]. The Mn^{n+} ions exist in the skeleton of octahedral molecular sieves with various oxidation states, and the K^{1+} ions exist in the center of the channel surrounded by [MnO_6] octahedra to maintain the overall charge balance. Manganese oxide octahedral molecular sieves have special strictures; therefore, these materials can be modified by structure construction, facet engineering, morphology control, and element doping. The manganese oxide octahedral molecular sieves have gotten considerable interest in catalytic applications for environmental remediation [45,46]. However, manganese oxide is a narrow band gap semiconductor, therefore it is not successful in photocatalytic applications under visible light irradiation due to the quick recombination of photoinduced positive holes and electrons. The photocatalytic performance of manganese oxide under visible light irradiation can be improved by increasing the lifetime of positive holes and electrons [47]. Therefore, in this study, we deposited Ag nanoparticles on the surface of manganese oxide to get a visible light-responsive photocatalyst for the crystal violet dye degradation. The charge transfer and synergetic effect expected by the deposition of Ag nanoparticles on the surface of manganese oxide result in an increase in the photocatalytic performance of Ag-MnO_2 in the photodegradation of crystal violet dye. Crystal violet dye has been used in a wide range of applications, such as dye processing, medicine, dermatological agents, biological staining, printing, textiles, etc. It is a synthetic cationic dye and belongs to the triphenyl methane family. Being a cationic dye, it easily penetrates the cell due to its interaction with the negatively charged surface of the membrane. The inhalation of crystal violet dye causes dizziness, diarrhea, and vomiting [48].

2. Experimental Section

2.1. Synthesis of Manganese Oxide OMS

An acidic precipitation experimental procedure was followed for the synthesis of manganese oxide OMS. For this purpose, two solutions were prepared: one by taking 14 g of potassium permanganate (Sigma-Aldrich, St. Louis, MO, USA) in 250 mL of distilled water, and the other by taking 21 g manganese acetate (Merck, Rahway, NJ, USA) in a mixture of 190 mL of distilled water and 10 mL of nitric acid (Sigma-Aldrich). Then, both solutions were mixed by dropwise addition of the solution of potassium permanganate to the solution of manganese acetate. Later, the resultant mixed solution was refluxed for 24 h. The reflux created a precipitate in the reaction mixture. The precipitate formed was filtered, washed, and dried at 110 °C for 10 h. Finally, the manganese oxide OMS formed was ground and stored for further analysis. It was designated as OMS.

2.2. Synthesis of Ag-Decorated Manganese Oxide OMS

Ag-decorated manganese oxide OMS was prepared using the green method using leaf extracts of *Calotropis gigantea*. Leaf extracts were prepared by refluxing dried and washed leaves of *Calotropis gigantea* for 2 h, followed by filtration. Typically, 0.314 g of silver nitrate (Merck) is taken in 100 mL of distilled water. Then, 1.686 g of previously prepared manganese oxide OMS was added to a solution of silver nitrate. Finally, 150 mL of leaf extracts were added to the reaction mixture and stirred for 2 h, followed by filtration and drying. The prepared substance was designated as Ag-OMS.

2.3. Characterization

The fabricated material was characterized with X-ray diffraction spectroscopy, scanning electron microscopy, energy dispersive X-ray spectroscopy, thermal gravimetric analysis, and Fourier transform infrared analysis using JDX-3532-JEOL, JSM-5910-JEOL, JDX-3532-JEOL, and TGA-7 Perkin Elmer models and Bruker VRTEX70, respectively.

2.4. Photocatalysis

Various degradation experiments were performed for the evaluation of photocatalytic activities of fabricated OMS and Ag-OMS. An aqueous solution of crystal violet dye (commercial grade) was used as a model contaminant. The degradation experiments were performed under the irradiation of sunlight using model wastewater contaminated with crystal violet dye. The extent of photodegradation was observed by measuring the absorbance of crystal violet dye at λ_{max} 583 nm using a UV-visible spectrophotometer (LAMBDA 1050+, PerkinElmer, Waltham, MA, USA). The measure of absorbance was used for the calculation of the concentration of dye solution using a previously prepared standard curve. Before the measurement of the photocatalytic activity of Ag-OMS, two blank experiments were also conducted. The first blank experiment was conducted to find out the degradation of crystal violet dye due to the absorption of light, i.e., photolysis. For this purpose, a solution of crystal violet dye was taken in a Pyrex glass beaker and stirred for one hour in sunlight. The solution was then analyzed for any change in concentration. The second blank experiment was conducted to find out the contribution of adsorption to the removal of crystal violet dye. For this purpose, a known mass of catalyst was suspended in the solution of crystal violet dye, and then the mixture was stirred under dark conditions for one hour. Then, the solution was analyzed for changes in the concentration of dye.

3. Results and Discussion

3.1. Synthesis

Manganese oxide was prepared by the precipitation method under acidic conditions using potassium permanganate and manganese (III) acetate as precursor substances. Manganese oxide was formed as follows:

$$MnO_2^{1-} + Mn^{3+} \rightarrow 2MnO_2$$

Ag nanoparticles were deposited on manganese oxide by a green method using the leaf extract of *Calotropis gigantea* as a reducing agent. The Leaf extract of *Calotropis gigantea* contains a wide range of phytochemicals, including flavonoids, gigantin, glycosides, phenolics, saponins, and many more. These phytochemicals have great potential for the reduction of silver ions and the stabilization of reduced silver nanoparticles [49–52]. The fabrication of Ag-decorated manganese oxide can be represented as follows:

$$MnO_2 + Ag^{1+} + \text{Phytochemicals} \rightarrow Ag - MnO_2$$

3.2. Characterization

The crystal structure of fabricated OMS and Ag-OMS was determined by XRD analysis. As given in Figure 2, the XRD of both OMS and Ag-OMS consists of sharp peaks that confirm the crystallinity of the fabricated material. The diffraction signals at 2θ = 28.35°, 37.75°, 40.93°, 42.13°, 56.35°, 59.27°, 65.65°, 67.23°, and 72.39° represent the existence of β-MnO_2. These peaks correspond to [1-1-0], [1-0-1], [2-0-0], [1-1-1], [2-1-1], [2-2-0], [0-0-2], [3-1-0], and [3-0-1] hkl planes of the tetragonal unit cell of β-MnO_2, respectively [53–56]. The observed XRD pattern could be radially indexed to tetragonal MnO (1 × 1) pyrolusite (β-MnO_2) (JCPDS 24-0735) [41]. The lattice parameters (a, b, c), Miller indices (h, k, l), and interplanar spacing (d_{hkl}) for the tetragonal unit call are related as given in Equation (1). The interplanar spacing is related to the angle of diffraction as $d_{hkl} = 1.5406/(2\text{Sin}\theta)$. The observed angles of diffraction and hkl planes given in XRD were treated according to Equation (1) by the nonlinear method for the calculation of lattice parameters. The Solver add-in of the Excel program was followed for the calculations by the non-linear method. The average lattice parameters were a = b = 1.34 Å and c = 2.74 Å. The additional diffraction signal observed in Figure 2b at 2θ = 38.65°, 44.15°, and 64.15° has been indexed to [1-1-1], [2-0-0], [2-2-0], and [2-2-2] hkl crystal planes of Ag, respectively (JCPDS: 04-0783). Hence, the XRD analyses show that Ag has been successfully supported on MnO_2 [57–59]. Based on XRD analysis, the fabricated OMS and Ag-OMS are considered pure and crystalline substances.

$$\frac{1}{d_{hkl}^2} = \frac{h^2 + k^2}{a^2} + \frac{l^2}{c^2} \tag{1}$$

The shapes and morphologies of the particles of OMS and Ag-OMS were studied by scanning electron microscopy. The SEM images of OMS and Ag-OMS particles are given in Figure 3. It can be observed that OMS exists in the form of rods with a diameter of approximately 100 nm (Figure 3a). The SEM images show that the rods of OMS are homogeneous and non-agglomerated in nature. The homogeneous morphology of the catalysts plays an important role in reproducing the same photocatalytic results. The non-agglomerated nature of catalyst particles is also very important because nonagglomerated catalyst particles are easily accessible to reactant molecules. Lachheb and coworkers [60] have reported mesoporous α-MnO2 with rod-like morphology. They reported that rod-shaped particles provide easily accessible sites for the reactant molecules. The SEM images of Ag-OMS (Figure 3b) show that particles of Ag and OMS are spherical rod-shaped in morphology, respectively. The SEM analysis confirms the successful deposition, coating, and dispersion of Ag nanoparticles at the surface of OMS. Furthermore, it is observed that OMS retains its shape and morphology in Ag-OMS.

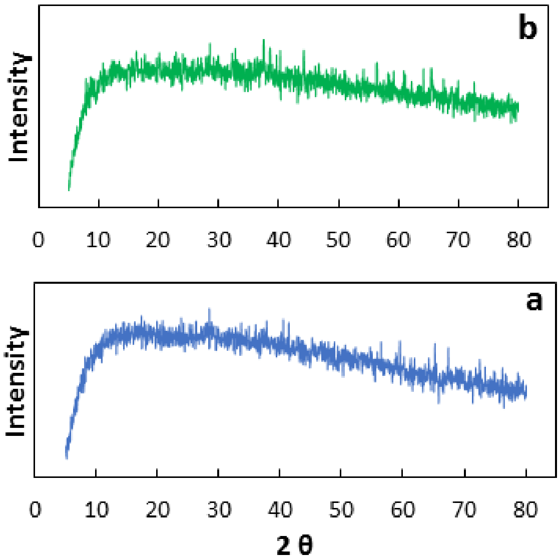

Figure 2. XRD of OMS (**a**) and Ag-OMS (**b**).

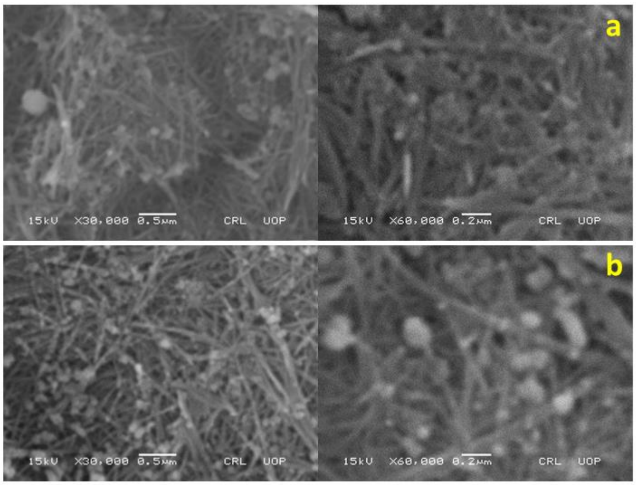

Figure 3. SEM images of OMS (**a**) and Ag-OMS (**b**) at different magnifications.

The elemental composition of OMS and Ag-OMS was confirmed by EDX analysis. Figure 4 shows the EDX spectra of the samples. The EDX of OMS confirms the existence of Mn, O, and K. Hence, it suggests the successful fabrication of manganese oxide OMS. The existence of a signal for C is suggested as an impurity in the precursor or contamination during the experimental process. Similarly, the EDX of Ag-decorated manganese oxide OMS confirms the existence of Ag, Mn, O, and K, along with impure elements. The XRD and EDX analyses support the successful fabrication of the target material.

Thermal measurements for the OMS and Ag-OMS were studied with thermal gravimetric analysis (TGA) and thermal differential analysis (DTA). The measurements were carried out by taking a known mass of OMS and Ag-OMS in the range of 30–700 °C at 10 °C/min in a nitrogen atmosphere. Figure 5 depicts the TGA and DTA of OMS and Ag-OMS. The TGA profile of OMS shows three steps of weight loss. A loss of ~2% in the mass of OMS was observed before 140 °C in the first step. This loss is associated with the elimination of surface-bound water. The second step consists of a ~3% loss in the mass of OMS before 300 °C, which is associated with the elimination of lattice oxygen and the phase transformation of MnO_2 to Mn_2O_3. Then there was no appreciable loss in mass up to 530 °C. However, a further loss of ~3% in the mass of OMS was observed in the temperature range 530–700 °C, representing additional elimination of lattice oxygen and phase transformation of Mn_2O_3 to Mn_3O_4 [61–63]. A similar TGA profile was observed for

Ag-OMS as well; however, the loss in mass before 300 °C was slightly higher (~4%), which might be due to the decomposition of unwashed plant material. The DTA of both OMS and Ag-OMS consists of exothermic and endothermic portions before and after 230 °C, respectively. These positions have been assigned to the elimination of water or plant contents and phase transformations, respectively.

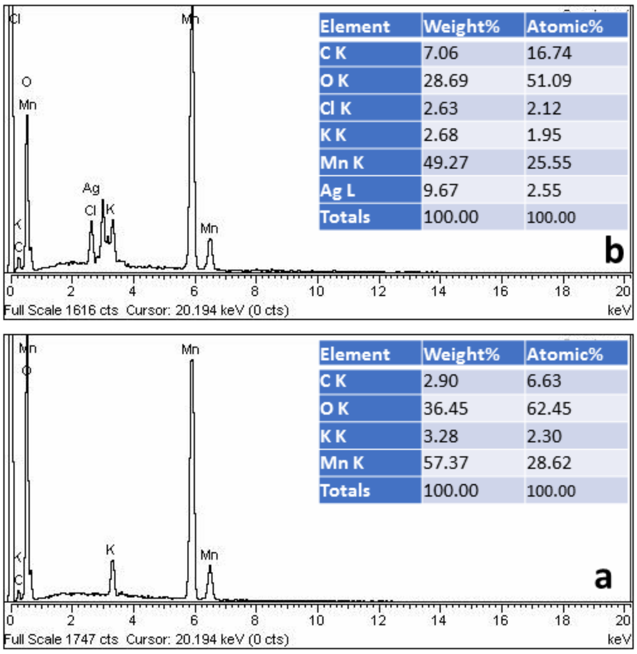

Element	Weight%	Atomic%
C K	7.06	16.74
O K	28.69	51.09
Cl K	2.63	2.12
K K	2.68	1.95
Mn K	49.27	25.55
Ag L	9.67	2.55
Totals	100.00	100.00

Element	Weight%	Atomic%
C K	2.90	6.63
O K	36.45	62.45
K K	3.28	2.30
Mn K	57.37	28.62
Totals	100.00	100.00

Figure 4. EDX of OMS (**a**) and Ag-OMS (**b**).

FTIR spectra of OMS and Ag-OMS showed bands at 178, 429, 543, 567, 578, 649, 659, and 720 cm^{-1}, representing the vibrations of Mn-O linkages in MnO_6 octahedral units. The absorption bands near 1600 and 2300 cm^{-1} represent the vibration of the hydroxyl group or water molecules in the tunnel of OMS. The absorption band for Ag-Ag metallic bond vibrations could not be observed in the FTIR spectrum of Ag-OMS because this bond shows vibrations below 400 cm^{-1} (Figure 6) [53,64,65].

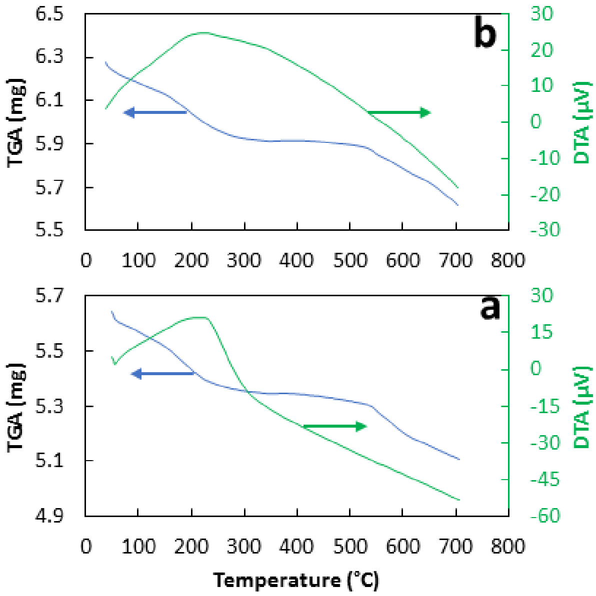

Figure 5. Thermal analysis of OMS (**a**) and Ag-OMS (**b**).

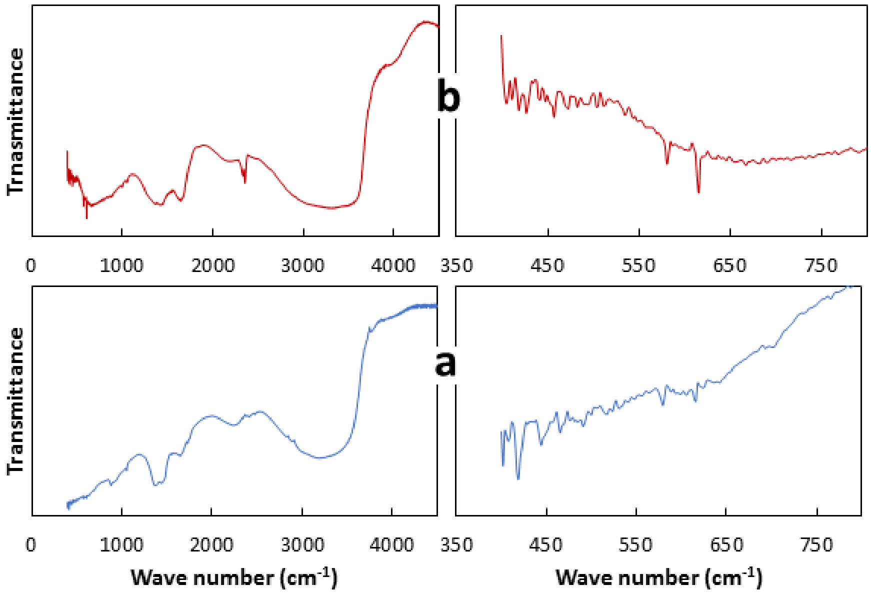

Figure 6. FTIR analysis of OMS (**a**) and Ag-OMS (**b**).

3.3. Photocatalysis

The photocatalytic performance of prepared OMS and Ag-OMS was evaluated by performing photodegradation experiments using crystal violet dye as a model pollutant. A 100 mg/L solution of dye (50 mL) was used for the measurement of the photocatalytic performance of different catalyst samples. The photocatalytic degradation study was accomplished in three steps.

First, the degradation of crystal violet dye due to sunlight was evaluated. For this purpose, a solution of crystal violet dye was taken in a Pyrex glass beaker and stirred for one hour under sunlight. Before stirring under sunlight, a sample of dye solution was taken, and its absorbance was measured using a spectrophotometer. After stirring for one hour, another sample of dye solution was taken, and its absorbance was measured. It was noted that there was no difference in the absorbance values taken before and after stirring the dye solution in sunlight. These results show there is no degradation (photolysis) of crystal violet dye due to sunlight alone.

In the second step, an optimum amount of OMS or Ag-OMS (0.8 g) was suspended in the solution of crystal violet dye, and then the mixture was stirred under dark conditions for one hour. A 0.5-mL sample was taken after 15, 30, 45, and 60 min. The absorbance of each sample was measured. The analysis of the obtained results showed that there was approximately a 25% decrease in the concentration of crystal violet dye. This decrease in the concentration of crystal violet dye is attributed to sorption on the surface of OMS. The absorbance measured after the one-hour stirring of a dye solution containing OMS or Ag-OMS was used as the initial absorbance for the investigations in the third step.

In the third step, the dye solution containing OMS or Ag-OMS was stirred continuously under sunlight for two hours. Samples were taken after every 15 min, and the absorbance of each sample was measured using a spectrophotometer. The extent of photodegradation was calculated using the Beer-Lambert law, according to which the change in concentration of crystal violet dye (C/C_o, C_o = 100 mg/L) is proportional to the normalized absorption value (A/A_o) as given in Figure 7a. The data given in Figure 7a shows that the deposition of Ag on OMS enhances the photocatalytic performance of OMS. For optimization of Ag content, three Ag-OMS photocatalysts having 5, 10, and 15% Ag (designated as 5-Ag-OMS, 10-Ag-OMS, and 15-Ag-OMS) were prepared and used as photocatalysts for the degradation of crystal violet dye. The photocatalytic performance of OMS, 5-Ag-OMS, 10-Ag-OMS, and 15-Ag-OMS was found to be 68, 79, 95, and 85%, respectively. The reaction time for 50% photodegradation for OMS was 75 min whereas it decreased to 58, 35, and

42 min for 5-Ag-OMS, 10-Ag-OMS, and 15-Ag-OMS, respectively. The photodegradation data of crystal violet dye were further investigated by pseudo first-order kinetic analyses. Figure 7b depicts the results of kinetics analyses. The kinetic parameters are given in Table 1. The photocatalytic performance of Ag-OMS increased with an increase in Ag content from 5 to 10%. However, beyond 10% loading of Ag, the photocatalytic activity of Ag-OMS decreased. It shows that the overloading of Ag content causes a decrease in photocatalytic performance. The decrease in photocatalytic performance of Ag-OMS with overloading of Ag content is attributed to the formation of an aggregation effect, which is responsible for inhibition in the physical contact between Ag and OMS [66]. These results show that Ag-OMS loaded with 10% Ag exhibits the best photocatalytic performance in this study. Therefore, this sample was used in further analyses and characterization. The obtained results show that Ag nanoparticles play a positive role in the photodegradation of crystal violet dye.

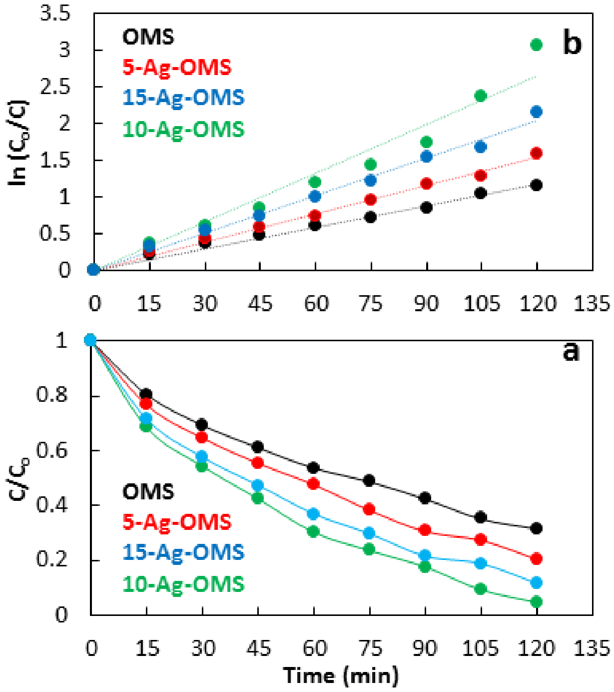

Figure 7. Photocatalytic degradation of crystal violet dye over different samples of Ag-OMS catalyst (Crystal violet dye; 100 mg/L, 50 mL; Catalyst: 0.08 g). (**a**) Photo catalytic activity; (**b**) Kinetics analysis.

Table 1. Kinetic parameters of OMS and Ag-OMSs catalyzed photodegradation of crystal violet dye.

Photocatalyst	Rate Constant (min^{-1})	R^2	Activity (%)
OMS	0.009	0.996	68
5-Ag-OMS	0.013	0.998	79
10-Ag-OMS	0.022	0.986	95
15-Ag-OMS	0.017	0.997	85

The optimization of the photocatalyst dosage is a crucial factor because it significantly affects the efficiency of the photodegradation reaction. For optimization of photocatalyst dosage, separate degradation experiments on crystal violet dye were performed with various dosages of 10-Ag-OMS in the range of 0.02 to 0.1 g while keeping the other parameters the same. The analyses of results showed that an increase in the amount of 10-Ag-OMS caused an increase in the rate of photodegradation reaction up to 0.08 g. There was no significant increase in the rate of reaction beyond the 0.08 g of the photocatalyst. The maximum degradation performance was observed at 0.08 g of photocatalyst hence this loading of catalyst was considered as optimum dosage and used in further reactions. The overloading of photocatalysts produces a negative impact on photocatalytic performance. The higher catalyst dosage diminishes the penetration of light to the surface of the catalyst by unfavorable light scattering.

The stability and reusability of the photocatalyst are also crucial factors in practical applications. The best catalyst is the one that can be recycled many times before its deactivation. The reusability was evaluated by using spent 10-Ag-OMS in three consecutive photodegradation experiments. The spent catalyst was washed with ethanol and then with water. After washing, it dried at 100 °C for 12 h. Then, it was re-employed as a catalyst in the photodegradation experiment of crystal violet dye. The photocatalytic activity was found to be higher than 90% in all recycled experiments. Hence, the photocatalyst reported in this study is stable and can be recycled many times in photodegradation experiments.

The initial concentration of dye also affects the photocatalytic performance. Therefore, separate photodegradation experiments were performed using 50, 100, and 150 mg/L solutions of crystal violet dye under identical experimental conditions. The obtained data were analyzed using a pseudo-first-order kinetics model. The obtained results are given in Table 2. The data given in Table 2 show that the photocatalytic performance of 10-Ag-OMS is inversely proportional to the initial concentration of crystal violet dye. At higher concentrations of dye, the photon cannot reach effectively the surface of the photocatalyst due to the scattering and absorption of photons by dye molecules.

Table 2. Effect of the concentration of crystal violet dye on the photocatalytic performance of 10-Ag-OMS.

Crystal Violet Dye (mg/L)	**Rate Constant (min^{-1})**	**R^2**	**Activity (%)**
50	0.036	0.978	100 *
100	0.022	0.986	95 **
150	0.011	0.997	71 **

Note: * 75 and ** 120 min reaction duration, respectively.

3.4. Mechanism of the Photocatalytic Process

The enhanced photocatalytic performance of Ag-OMS is due to the efficient harvesting of sunlight on its exterior. Pristine OMS absorbs photons in the ultraviolet (edge at ~335 nm) and near infra-red (~650–825 nm) regions. For the Ag-OMS junction, the surface plasmon phenomenon shifts the absorption to the visible region (edge at ~490 nm) and enhances the absorption in the near-infrared region (600–1100 nm) as well. Hence, Ag-OMS efficiently harvests sunlight. Figure 8 explains the photocatalytic process. The absorbed sunlight causes the excitation of photoelectrons from the valence band of OMS to its conduction band. The interfacial connection of OMS (MnO_2) with Ag creates a Schottky junction that causes an efficient separation of photogenerated electrons and positive holes. As a result of efficient separation due to the Schottky junction, the rate of recombination of electrons and positive holes diminishes and ultimately enhances photocatalytic performance [67–69]. The separated photogenerated positive holes and electrons initiate a series of redox reactions and produce OH radicals that mineralize the molecules of crystal violet dye. These redox reactions are given below.

$$\mathrm{Ag-OMS + h\vartheta \rightarrow Ag-OMS\ \left(h^{+}+e^{-}\right)}$$

$$\mathrm{Ag-OMS + h\vartheta \rightarrow Ag-OMS\ \left(h^{+}+e^{-}\right)}$$

$$\mathrm{Ag-OMS\ \left(h^{+}+e^{-}\right) \rightarrow OMS\ \left(h^{+}\right) + Ag\ \left(e^{-}\right)}$$

$$\mathrm{OMS\ \left(h^{+}\right) + H_2O\ \rightarrow OH^{\bullet}}$$

$$\mathrm{Ag\ \left(e^{-}\right) +\ O_2\ \rightarrow\ O_2^{\bullet -}}$$

$$O_2^{\bullet -} + H^+ \rightarrow HO_2^{\bullet}$$

$$HO_2^{\bullet} \rightarrow OH^{\bullet}$$

$$CV + OMS\left(h^+\right) + Ag\left(e^-\right) + OH^{\bullet} + O_2^{\bullet -} + HO_2^{\bullet} \rightarrow \text{Degradation products}$$

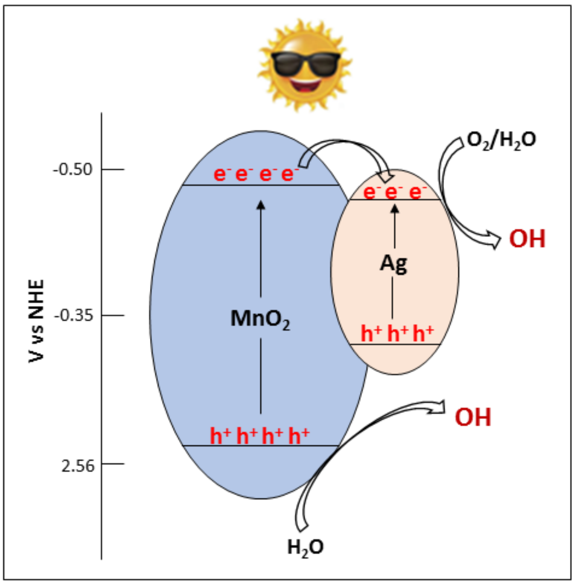

Figure 8. Mechanism of the photocatalytic process.

The proposed mechanism was tested with a trapping experimental system. For this purpose, ammonium oxalate, benzoquinone, and tertiary butanol were used as scavengers for positive holes, superoxide anion radicals, and hydroxyl radicals, respectively. Photocatalytic performance was significantly impaired in the presence of benzoquinone and tertiary butanol; however, there was no significant effect of ammonium oxalate on the photocatalytic performance. This testifies that superoxide anion radicals and hydroxyl radicals are the key species taking part in the mineralization of crystal violet dye [70–72].

The photocatalytic results of this study show that Ag-OMS may effectively catalyze water molecules and oxygen molecules into hydroxyl radicals under the irradiation of sunlight. It has been reported earlier that MnO_2 nanowires have shown promising performance in the dye's degradation due to the potential of MnO_2 for the activation of oxygen molecules [64]. Kong et al. have reported the reduction of oxygen by reaction with photo-induced electrons and the oxidation of water by reaction with photo-induced positive holes under irradiation of ultraviolet light [73].

Similarly, Wang and his co-workers have suggested that water molecules present in the reaction mixture and the tunnel of MnO_2 rods are responsible for the production of hydroxyl radicals, due to which the breaking of the dye azo linkage (−N=N−) becomes easier [74]. The involvement of the breaking of azo linkage (−N=N−) in photodegradation is evident in the higher degradation rate of Congo red dye than the photodegradation rate of methyl orange, as reported by Lachheb and coworkers [60]. They attributed the higher degradation rate of Congo red dye to the availability of two reaction sites in the dye (−N=N−) because the hydroxyl radicals can easily attack these active sites of the dye molecule.

4. Conclusions

In summary, manganese oxide octahedral molecular sieves designated as OMS and Ag-decorated manganese oxide octahedral molecular sieves designated as Ag-OMS were successfully synthesized and utilized for the photodegradation of a model pollutant, crystal violet dye. The XRD analysis confirmed the successful fabrication of β-MnO_2 and Ag-decorated β-MnO_2 designated as OMS and Ah-OMS, respectively. The EDX analysis verified the existence of Ag, Mn, O, and K, along with impure elements. The XRD and EDX analyses support the successful fabrication of the target material. The results established that an optimum Ag-OMS showed outstanding photocatalytic performance in visible light-assisted degradation of crystal violet dye. Approximately 100, 95, and 75% photodegradation of 50, 100, and 150 mg/L crystal violet dye was observed in 90, 120, and 120 min in the presence of 10% Ag-OMS, respectively. The outstanding photocatalytic performance of Ag-OMS is attributed to the efficient separation of photogenerated positive holes and electrons. Furthermore, the mechanism of the photocatalytic process demonstrated that hydroxyl and superoxide anion radicals play a key role in the mineralization of organic pollutants. Therefore, the present study offers an efficient and facile photocatalyst for the treatment of real wastewater in the future.

Author Contributions: Conceptualization, M.S.; Methodology, M.S. and U.H.B.; Validation, M.S., R.D.C.P. and S.P.; Formal analysis, U.H.B.; investigation, M.S.; data curation, M.S.; writing—original draft preparation, M.S.; writing—revise and editing, S.K.A.; supervision, M.S.; funding acquisition, S.K.A., L.A.A.-S. and K.M.A.S. All authors have read and agreed to the published version of the manuscript.

Funding: This research was funded by Princess Nourah bint Abdulrahman University, (Grant No. PNURSP2023R365); and King Khalid University, (Grant No. R.G.P.2/345/44).

Data Availability Statement: Not applicable.

Acknowledgments: This research was funded by Princess Nourah bint Abdulrahman University Researchers Supporting Project number (PNURSP2023R365), Princess Nourah bint Abdulrahman University, Riyadh, Saudi Arabia, and the Deanship of Scientific Research of King Khalid University, Abha, Saudi Arabia, under grant number (RGP2/345/44) is fully acknowledged.

Conflicts of Interest: The authors declare no conflict of interest.

References

1. Miao, C.; Li, P.; Huang, Y.; Sun, Y.; Chen, W.; Yu, S. Coupling Outdoor Air Quality with Thermal Comfort in the Presence of Street Trees: A Pilot Investigation in Shenyang, Northeast China. *J. For. Res.* **2022**, *34*, 831–839. [CrossRef]
2. Agathokleous, S.; Saitanis, C.J.; Savvides, C.; Sicard, P.; Agathokleous, E.; De Marco, A. Spatiotemporal Variations of Ozone Exposure and Its Risks to Vegetation and Human Health in Cyprus: An Analysis across a Gradient of Altitudes. *J. For. Res.* **2022**, *34*, 579–594. [CrossRef]
3. Arshad, M.; Qayyum, A.; Abbas, G.; Haider, R.; Iqbal, M.; Nazir, A. Influence of Different Solvents on Portrayal and Photocatalytic Activity of Tin-Doped Zinc Oxide Nanoparticles. *J. Mol. Liq.* **2018**, *260*, 272–278. [CrossRef]
4. Thao, L.T.S.; Dang, T.T.T.; Khanitchaidecha, W.; Channei, D.; Nakaruk, A. Photocatalytic Degradation of Organic Dye under UV-A Irradiation Using TiO_2-Vetiver Multifunctional Nano Particles. *Materials* **2017**, *10*, 122. [CrossRef] [PubMed]
5. Kausar, A.; Naeem, K.; Tariq, M.; Nazli, Z.I.H.; Bhatti, H.N.; Jubeen, F.; Nazir, A.; Iqbal, M. Preparation and Characterization of Chitosan/Clay Composite for Direct Rose FRN Dye Removal from Aqueous Media: Comparison of Linear and Non-Linear Regression Methods. *J. Mater. Res. Technol.* **2019**, *8*, 1161–1174. [CrossRef]
6. Kamran, U.; Rhee, K.Y.; Lee, S.Y.; Park, S.J. Innovative Progress in Graphene Derivative-Based Composite Hybrid Membranes for the Removal of Contaminants in Wastewater: A Review. *Chemosphere* **2022**, *306*, 135590. [CrossRef] [PubMed]
7. Kamran, U.; Lee, S.Y.; Rhee, K.Y.; Park, S.J. Rice Husk Valorization into Sustainable Ni@TiO_2/Biochar Nanocomposite for Highly Selective Pb (II) Ions Removal from an Aqueous Media. *Chemosphere* **2023**, *323*, 138210. [CrossRef] [PubMed]
8. Wei, S.; Chen, T.; Hou, H.; Xu, Y. Recent Advances in Electrochemical Sterilization. *J. Electroanal. Chem.* **2023**, *937*, 117419. [CrossRef]
9. Li, M.; Xia, Q.; Lv, S.; Tong, J.; Wang, Z.; Nie, Q.; Yang, J. Enhanced CO_2 Capture for Photosynthetic Lycopene Production in Engineered Rhodopseudomonas Palustris, a Purple Nonsulfur Bacterium. *Green Chem.* **2022**, *24*, 7500–7518. [CrossRef]
10. Padervand, M.; Heidarpour, H.; Bargahi, A. A Mechanistic Study and In-Vivo Toxicity Bioassay on Acetamiprid Photodegradation over the Zeolite Supported Cerium-Based Photocatalyst. *J. Photochem. Photobiol. A Chem.* **2020**, *395*, 112526. [CrossRef]
11. Salari, H. Efficient Photocatalytic Degradation of Environmental Pollutant with Enhanced Photocarrier Separation in Novel Z-Scheme a-MnO_2 Nanorod/a-MoO_3 Nanocomposites. *J. Photochem. Photobiol. A Chem.* **2020**, *401*, 112787. [CrossRef]
12. Wang, Z.; Liu, X.; Ni, S.Q.; Zhuang, X.; Lee, T. Nano Zero-Valent Iron Improves Anammox Activity by Promoting the Activity of Quorum Sensing System. *Water Res.* **2021**, *202*, 117491. [CrossRef] [PubMed]

13. Yu, S.; Pang, H.; Huang, S.; Tang, H.; Wang, S.; Qiu, M.; Chen, Z.; Yang, H.; Song, G.; Fu, D.; et al. Recent Advances in Metal-Organic Framework Membranes for Water Treatment: A Review. *Sci. Total Environ.* **2021**, *800*, 149662. [CrossRef]
14. Hao, M.; Qiu, M.; Yang, H.; Hu, B.; Wang, X. Recent Advances on Preparation and Environmental Applications of MOF-Derived Carbons in Catalysis. *Sci. Total Environ.* **2021**, *760*, 143333. [CrossRef] [PubMed]
15. Qiu, M.; Liu, L.; Ling, Q.; Cai, Y.; Yu, S.; Wang, S.; Fu, D.; Hu, B.; Wang, X. Biochar for the Removal of Contaminants from Soil and Water: A Review. *Biochar* **2022**, *4*, 19. [CrossRef]
16. Kamran, U.; Bhatti, H.N.; Iqbal, M.; Jamil, S.; Zahid, M. Biogenic Synthesis, Characterization and Investigation of Photocatalytic and Antimicrobial Activity of Manganese Nanoparticles Synthesized from Cinnamomum Verum Bark Extract. *J. Mol. Struct.* **2019**, *1179*, 532–539. [CrossRef]
17. Li, G.; Huang, S.; Li, K.; Zhu, N.; Zhao, B.; Zhong, Q.; Zhang, Z.; Ge, D.; Wang, D. Near-Infrared Responsive Z-Scheme Heterojunction with Strong Stability and Ultra-High Quantum Efficiency Constructed by Lanthanide-Doped Glass. *Appl. Catal. B* **2022**, *311*, 121363. [CrossRef]
18. Khan, S.B.; Irfan, S.; Lam, S.S.; Sun, X.; Chen, S. 3D Printed Nanofiltration Membrane Technology for Waste Water Distillation. *J. Water Process Eng.* **2022**, *49*, 102958. [CrossRef]
19. Yu, H.; Zhu, J.; Qiao, R.; Zhao, N.; Zhao, M.; Kong, L. Facile Preparation and Controllable Absorption of a Composite Based on PMo_{12}/Ag Nanoparticles: Photodegradation Activity and Mechanism". *ChemistrySelect* **2022**, *7*, e202103668. [CrossRef]
20. Mo, X.; Liu, X.; Chen, J.; Zhu, S.; Xu, W.; Tan, K.; Wang, Q.; Lin, Z.; Liu, W. Separation of Lattice-Incorporated Cr(vi) from Calcium Carbonate by Converting Microcrystals into Nanocrystals via the Carbonation Pathway Based on the Density Functional Theory Study of Incorporation Energy. *Environ. Sci. Nano* **2022**, *9*, 1617–1626. [CrossRef]
21. Kamran, U.; Bhatti, H.N.; Noreen, S.; Tahir, M.A.; Park, S.J. Chemically Modified Sugarcane Bagasse-Based Biocomposites for Efficient Removal of Acid Red 1 Dye: Kinetics, Isotherms, Thermodynamics, and Desorption Studies. *Chemosphere* **2022**, *291*, 132796. [CrossRef] [PubMed]
22. Xu, P.; Ding, C.; Li, Z.; Yu, R.; Cui, H.; Gao, S. Photocatalytic Degradation of Air Pollutant by Modified Nano Titanium Oxide (TiO_2)in a Fluidized Bed Photoreactor: Optimizing and Kinetic Modeling. *Chemosphere* **2023**, *319*, 137995. [CrossRef] [PubMed]
23. Haounati, R.; Ighnih, H.; Ouachtak, H.; Eshaghi Malekshah, R.; Hafid, N.; Jada, A.; Ait Addi, A. Z-Scheme G-C_3n_4/Fe_3O_4/Ag_3PO_4@Sep Magnetic Nanocomposites as Heterojunction Photocatalysts for Green Malachite Degradation and Dynamic Molecular Studies. *SSRN Electron. J.* **2023**, *671*, 131509. [CrossRef]
24. Haounati, R.; Ighnih, H.; Malekshah, R.E.; Alahiane, S.; Alakhras, F.; Alabbad, E.; Alghamdi, H.; Ouachtak, H.; Addi, A.A.; Jada, A. Exploring ZnO/Montmorillonite Photocatalysts for the Removal of Hazardous RhB Dye: A Combined Study Using Molecular Dynamics Simulations and Experiments. *Mater. Today Commun.* **2023**, *35*, 105915. [CrossRef]
25. Li, X.; Xiong, J.; Gao, X.; Ma, J.; Chen, Z.; Kang, B.; Liu, J.; Li, H.; Feng, Z.; Huang, J. Novel BP/BiOBr S-Scheme Nano-Heterojunction for Enhanced Visible-Light Photocatalytic Tetracycline Removal and Oxygen Evolution Activity. *J. Hazard. Mater.* **2020**, *387*, 121690. [CrossRef]
26. Phillips, R.B.; James, R.R.; Magnuson, M.L. Functional Categories of Microbial Toxicity Resulting from Three Advanced Oxidation Process Treatments during Management and Disposal of Contaminated Water. *Chemosphere* **2020**, *238*, 124550. [CrossRef]
27. Zhu, B.; Cheng, H.; Qin, Y.; Ma, J.; Kong, Y.; Komarneni, S. Copper Sulfide as an Excellent Co-Catalyst with $K_2S_2O_8$ for Dye Decomposition in Advanced Oxidation Process. *Sep. Purif. Technol.* **2020**, *233*, 116057. [CrossRef]
28. Warshagha, M.Z.A.; Muneer, M. Visible Light Active Boron Doped Phenyl-g-C_3N_4 Nanocomposites for Decomposition of Dyes. *Surf. Interfaces* **2021**, *26*, 101394. [CrossRef]
29. Li, H.; Zhao, S.; Zhang, W.; Du, H.; Yang, X.; Peng, Y.; Han, D.; Wang, B.; Li, Z. Efficient Esterification over Hierarchical Zr-Beta Zeolite Synthesized via Liquid-State Ion-Exchange Strategy. *Fuel* **2023**, *342*, 127786. [CrossRef]
30. Xia, G.; Zheng, Y.; Sun, Z.; Xia, S.; Ni, Z.; Yao, J. Fabrication of ZnAl-LDH Mixed Metal-Oxide Composites for Photocatalytic Degradation of 4-Chlorophenol. *Environ. Sci. Pollut. Res.* **2022**, *29*, 39441–39450. [CrossRef]
31. Zhou, T.; Du, J.; Wang, Z.; Xiao, G.; Luo, L.; Faheem, M.; Ling, H.; Bao, J. Degradation of Sulfamethoxazole by MnO_2/Heat-Activated Persulfate: Kinetics, Synergistic Effect and Reaction Mechanism. *Chem. Eng. J. Adv.* **2022**, *9*, 100200. [CrossRef]
32. Zhao, M.; Xu, R.; Chen, Z.; Gao, Z.; Zheng, S.; Song, H. Kinetics and Mechanisms of Diniconazole Degradation by α-MnO_2 Activated Peroxymonosulfate. *Sep. Purif. Technol.* **2022**, *281*, 119850. [CrossRef]
33. Zhang, X.; Zhang, C.; Lin, Q.; Cheng, B.; Liu, X.; Peng, F.; Ren, J. Preparation of Lignocellulose-Based Activated Carbon Paper as a Manganese Dioxide Carrier for Adsorption and in-Situ Catalytic Degradation of Formaldehyde. *Front. Chem.* **2019**, *7*, 808. [CrossRef] [PubMed]
34. Barreca, D.; Gri, F.; Gasparotto, A.; Altantzis, T.; Gombac, V.; Fornasiero, P.; Maccato, C. Insights into the Plasma-Assisted Fabrication and Nanoscopic Investigation of Tailored MnO_2 Nanomaterials. *Inorg. Chem.* **2018**, *57*, 14564–14573. [CrossRef] [PubMed]
35. Zhu, Y.; Shen, M.; Xia, Y.; Lu, M. Au/MnO_2 Nanostructured Catalysts and Their Catalytic Performance for the Oxidation of 5-(Hydroxymethyl)Furfural. *Catal. Commun.* **2015**, *64*, 37–43. [CrossRef]
36. Wang, S.; Guan, A.; Wang, J.; Fu, X.; Guo, X.; Tian, Y.; Wang, K.; Cao, W.; Zhao, C. Highly Efficient Degradation of Rhodamine B by α-MnO_2 Nanorods. *Bull. Mater. Sci.* **2022**, *45*, 35. [CrossRef]
37. Kamran, U.; Heo, Y.J.; Min, B.G.; In, I.; Park, S.J. Effect of Nickel Ion Doping in MnO_2/Reduced Graphene Oxide Nanocomposites for Lithium Adsorption and Recovery from Aqueous Media. *RSC Adv.* **2020**, *10*, 9245–9257. [CrossRef]

38. Huang, Z.; Gu, X.; Cao, Q.; Hu, P.; Hao, J.; Li, J.; Tang, X. Catalytically Active Single-Atom Sites Fabricated from Silver Particles. *Angew. Chem. Int. Ed.* **2012**, *51*, 4198–4203. [CrossRef]
39. Liu, P.; Duan, J.; Ye, Q.; Mei, F.; Shu, Z.; Chen, H. Promoting Effect of Unreducible Metal Doping on OMS-2 Catalysts for Gas-Phase Selective Oxidation of Ethanol. *J. Catal.* **2018**, *367*, 115–125. [CrossRef]
40. Huang, L.; Hu, X.; Yuan, S.; Li, H.; Yan, T.; Shi, L.; Zhang, D. Photocatalytic Preparation of Nanostructured MnO_2-(CO_3O_4)/TiO_2 Hybrids: The Formation Mechanism and Catalytic Application in SCR DeNOx Reaction. *Appl. Catal. B* **2017**, *203*, 778–788. [CrossRef]
41. Wang, X.; Tan, W.; Guo, K.; Ji, J.; Gao, F.; Tong, Q.; Dong, L. Evaluation of Manganese Oxide Octahedral Molecular Sieves for CO and C_3H_6 Oxidation at Diesel Exhaust Conditions. *Front. Environ. Chem.* **2021**, *2*, 672250. [CrossRef]
42. Turner, S.; Buseck, P.R. Todorokites: A New Family of Naturally Occurring Manganese Oxides. *Science* **1981**, *212*, 1024–1027. [CrossRef] [PubMed]
43. Feng, Q.; Kanoh, H.; Ooi, K. Manganese Oxide Porous Crystals. *J. Mater. Chem.* **1999**, *9*, 319–333. [CrossRef]
44. Kong, L.; Liu, Y.; Dong, L.; Zhang, L.; Qiao, L.; Wang, W.; You, H. Enhanced Red Luminescence in $CaAl_{12}O_{19}$:Mn_4+: Via Doping Ga_3+ for Plant Growth Lighting. *Dalton Trans.* **2020**, *49*, 1947–1954. [CrossRef] [PubMed]
45. Thenmozhi, E.; Harshavardhan, M.; Kamala-Kannan, S.; Janaki, V. Synthesis and Characterization of Mesoporous Silica-MnO_2 Nanocomposite—An Efficient Nanocatalyst for Methylene Blue Degradation. *Mater. Lett.* **2022**, *309*, 131367. [CrossRef]
46. Tong, W.; Wang, J.; Du, X.; Wang, X.; Wang, Y.; Zhang, Y. Tributyl Phosphate Degradation and Phosphorus Immobilization by MnO_2: Reaction Condition Optimization and Mechanism Exploration. *J. Hazard. Mater.* **2022**, *432*, 128725. [CrossRef]
47. Li, H.; Fu, B.; Huang, H.; Wu, S.; Ge, J.; Zhang, J.; Li, F.; Qu, P. Catalytic Degradation of Organic Pollutants by Manganese Oxides: A Comprehensive Review. *Environ. Pollut. Bioavailab.* **2022**, *34*, 395–406. [CrossRef]
48. Rahmat, M.; Rehman, A.; Rahmat, S.; Bhatti, H.N.; Iqbal, M.; Khan, W.S.; Bajwa, S.Z.; Rahmat, R.; Nazir, A. Highly Efficient Removal of Crystal Violet Dye from Water by MnO_2 Based Nanofibrous Mesh/Photocatalytic Process. *J. Mater. Res. Technol.* **2019**, *8*, 5149–5159. [CrossRef]
49. Saeed, M.; Muneer, M.; Mumtaz, N.; Siddique, M.; Akram, N.; Hamayun, M. Ag-CO_3O_4: Synthesis, Characterization and Evaluation of Its Photo-Catalytic Activity towards Degradation of Rhodamine B Dye in Aqueous Medium. *Chin. J. Chem. Eng.* **2018**, *26*, 1264–1269. [CrossRef]
50. Mittal, A.K.; Chisti, Y.; Banerjee, U.C. Synthesis of Metallic Nanoparticles Using Plant Extracts. *Biotechnol. Adv.* **2013**, *31*, 346–356. [CrossRef]
51. Singh, M.; Javed, K. Comparative Study of Chemical Composition of Calotropis Gigantea Flower, Leaf and Fruit. *Eur. Chem. Bull.* **2015**, *4*, 477–480.
52. Zafar, L.; Khan, A.; Kamran, U.; Park, S.J.; Bhatti, H.N. Eucalyptus (Camaldulensis) Bark-Based Composites for Efficient Basic Blue 41 Dye Biosorption from Aqueous Stream: Kinetics, Isothermal, and Thermodynamic Studies. *Surf. Interfaces* **2022**, *31*, 101897. [CrossRef]
53. Warshagha, M.Z.A.; Muneer, M. Direct Z-Scheme AgBr/β-MnO_2 Photocatalysts for Highly Efficient Photocatalytic and Anticancer Activity. *ACS Omega* **2022**, *7*, 30171–30183. [CrossRef] [PubMed]
54. Wang, L.; He, H.; Zhang, C.; Sun, L.; Liu, S.; Wang, S. Antimicrobial Activity of Silver Loaded MnO_2 Nanomaterials with Different Crystal Phases against Escherichia Coli. *J. Environ. Sci.* **2016**, *41*, 112–120. [CrossRef]
55. Wang, X.; Li, Y. Selected-Control Hydrothermal Synthesis of α- and β-MnO_2 Single Crystal Nanowires. *J. Am. Chem. Soc.* **2002**, *124*, 2880–2881. [CrossRef]
56. Mohamed Racik, K.K.; Prabakaran, P.; Madhavan, J.; Victor Antony Raj, M. Surfactant Free Hydrothermal Synthesis, Structural and Dielectric Studies of One-Dimensional $BmnO_2$ Nanorods. *Mater. Today Proc.* **2019**, *8*, 162–168. [CrossRef]
57. Luo, H.; Yang, Y.; Yang, B.; Xu, Z.; Wang, D. Silver/Manganese Dioxide Nanorod Catalyzed Hydrogen-Borrowing Reactions and Tert-Butyl Ester Synthesis. *J. Chem. Res.* **2021**, *45*, 708–715. [CrossRef]
58. Gao, X.; Shang, Y.; Liu, L.; Fu, F. Multilayer Ultrathin Ag-δ-Bi_2O_3 with Ultrafast Charge Transformation for Enhanced Photocatalytic Nitrogen Fixation. *J. Colloid Interface Sci.* **2019**, *533*, 649–657. [CrossRef]
59. Saeed, M.; Haq, A.U.; Muneer, M.; Ahmad, A.; Bokhari, T.H.; Sadiq, Q. Synthesis and Characterization of Bi_2O_3 and Ag-Bi_2O_3 and Evaluation of Their Photocatalytic Activities towards Photodegradation of Crystal Violet Dye. *Phys. Scr.* **2021**, *96*, 125707. [CrossRef]
60. Lachheb, H.; Puzenat, E.; Houas, A.; Ksibi, M.; Elaloui, E.; Guillard, C.; Herrmann, J.M. Photocatalytic Degradation of Various Types of Dyes (Alizarin S, Crocein Orange G, Methyl Red, Congo Red, Methylene Blue) in Water by UV-Irradiated Titania. *Appl. Catal. B* **2002**, *39*, 75–90. [CrossRef]
61. Chen, L.; Zhang, Q.; Xu, H.; Hou, X.; Xuan, L.; Jiang, Y.; Yuan, Y. Amorphous 3D Nanoflake Array-Assembled Porous 2D Cobalt-Oxalate Coordination Polymer Thin Sheets with Excellent Pseudocapacitive Performance. *J. Mater. Chem. A Mater.* **2015**, *3*, 1847–1852. [CrossRef]
62. Asiri, S.M.M.; Cevik, E.; Sabit, H.; Bozkurt, A. Alginate-Guided Size and Morphology-Controlled Synthesis of MnO_2 Nanoflakes. *Soft Mater.* **2020**, *18*, 46–54. [CrossRef]
63. Worku, A.K.; Ayele, D.W.; Habtu, N.G.; Yemata, T.A. Engineering CO_3O_4/MnO_2 Nanocomposite Materials for Oxygen Reduction Electrocatalysis. *Heliyon* **2021**, *7*, e08076. [CrossRef] [PubMed]

64. Alzahrani, S.A.; Al-Thabaiti, S.A.; Al-Arjan, W.S.; Malik, M.A.; Khan, Z. Preparation of Ultra Long α-MnO_2 and Ag@MnO_2 Nanoparticles by Seedless Approach and Their Photocatalytic Performance. *J. Mol. Struct.* **2017**, *1137*, 495–505. [CrossRef]
65. Kong, L.; Sun, H.; Nie, Y.; Yan, Y.; Wang, R.; Ding, Q.; Zhang, S.; Yu, H.; Luan, G. Luminescent Properties and Charge Compensator Effects of $SrMo_{0.5}W_{0.5}O_4{:}Eu^{3+}$ for White Light LEDs. *Molecules* **2023**, *28*, 2681. [CrossRef]
66. Saravanakumar, K.; Muthuraj, V.; Vadivel, S. Constructing Novel Ag Nanoparticles Anchored on MnO_2 Nanowires as an Efficient Visible Light Driven Photocatalyst. *RSC Adv.* **2016**, *6*, 61357–61366. [CrossRef]
67. Panimalar, S.; Logambal, S.; Thambidurai, R.; Inmozhi, C.; Uthrakumar, R.; Muthukumaran, A.; Rasheed, R.A.; Gatasheh, M.K.; Raja, A.; Kennedy, J.; et al. Effect of Ag Doped MnO_2 Nanostructures Suitable for Wastewater Treatment and Other Environmental Pollutant Applications. *Environ. Res.* **2022**, *205*, 112560. [CrossRef]
68. Magdalane, C.M.; Kanimozhi, K.; Arularasu, M.V.; Ramalingam, G.; Kaviyarasu, K. Self-Cleaning Mechanism of Synthesized SnO_2/TiO_2 Nanostructure for Photocatalytic Activity Application for Waste Water Treatment. *Surf. Interfaces* **2019**, *17*, 100346. [CrossRef]
69. Alhaji, N.M.I.; Nathiya, D.; Kaviyarasu, K.; Meshram, M.; Ayeshamariam, A. A Comparative Study of Structural and Photocatalytic Mechanism of $AgGaO_2$ Nanocomposites for Equilibrium and Kinetics Evaluation of Adsorption Parameters. *Surf. Interfaces* **2019**, *17*, 100375. [CrossRef]
70. Khan, I.; Luo, M.; Guo, L.; Khan, S.; Wang, C.; Khan, A.; Saeed, M.; Zaman, S.; Qi, K.; Liu, Q.L. Enhanced Visible-Light Photoactivities of Porous $LaFeO_3$ by Synchronously Doping Ni^{2+} and Coupling TS-1 for CO_2 reduction and 2,4,6-Trinitrophenol Degradation. *Catal. Sci. Technol.* **2021**, *11*, 6793–6803. [CrossRef]
71. Khan, I.; Sun, N.; Wang, Y.; Li, Z.; Qu, Y.; Jing, L. Synthesis of SnO_2/Yolk-Shell $LaFeO_3$ Nanocomposites as Efficient Visible-Light Photocatalysts for 2,4-Dichlorophenol Degradation. *Mater. Res. Bull.* **2020**, *127*, 110857. [CrossRef]
72. Khan, I.; Sun, N.; Zhang, Z.; Li, Z.; Humayun, M.; Ali, S.; Qu, Y.; Jing, L. Improved Visible-Light Photoactivities of Porous $LaFeO_3$ by Coupling with Nanosized Alkaline Earth Metal Oxides and Mechanism Insight. *Catal. Sci. Technol.* **2019**, *9*, 3149–3157. [CrossRef]
73. Kong, M.; Li, Y.; Chen, X.; Tian, T.; Fang, P.; Zheng, F.; Zhao, X. Tuning the Relative Concentration Ratio of Bulk Defects to Surface Defects in TiO_2 Nanocrystals Leads to High Photocatalytic Efficiency. *J. Am. Chem. Soc.* **2011**, *133*, 16414–16417. [CrossRef] [PubMed]
74. Wang, J.; Fan, X.M.; Tian, K.; Zhou, Z.W.; Wang, Y. Largely Improved Photocatalytic Properties of Ag/Tetrapod-like ZnO Nanocompounds Prepared with Different PEG Contents. *Appl. Surf. Sci.* **2011**, *257*, 7763–7770. [CrossRef]